FULL RESEARCH ARTICLE

Fracture mechanisms of selective laser sintered parts manufactured in build direction

J. Cronau[1] · **M. Krönert[2]** · **F. Engstler[1]**

Abstract

Selective laser sintering (SLS) is an additive manufacturing process that, in addition to rapid prototyping, is becoming increasingly popular to produce end-use parts. Predictable mechanical properties of the produced parts through this process is a desired primary goal. It has long been known that the mechanical properties especially the elongation at break of SLS components decrease in the build direction. In various test series with tensile specimen fabricated in build direction by SLS, it was found that, on the one hand, these have a very large scatter of the elongation at break, and, on the other hand, it was noticed that these frequently break outside the test range in the upskin radius. The upskin area describes regions that point in a positive build direction relative to the building plate. The fracture occurs at a point where, due to the specimen cross-section, a lower fracture stress occurs than in the test area of the specimen. This fracture leads to a much lower elongation at break than in the case of specimens that fracture in the test area. This study investigates which mechanism triggers this behavior. It turns out that different roughnesses can be determined in the upskin and downskin radius and different defects can be seen in the fracture surfaces, especially in the edge areas. It cannot be predicted based on surface roughness measurements or surface profiling exactly where, or in which layer the fracture occurs. However, the defects lead to a local stress spike, at which the failure of the specimen begins.

Keywords Selective laser sintering (SLS) · Surface roughness · Build direction · Fracture

1 Introduction

Primary advantages of additive manufacturing (AM) is that it eases the manufacturing of geometrically complex, functionally integrated and individualized parts [1–3]. Selective laser sintering, in particular, is considered as a technically mature and industrially relevant technology [4, 5]. As in many AM processes, three-dimensional components are sliced into individual layers in advance of the SLS process [1]. In the actual manufacturing process, the complete build platform is coated with powder in layers and selected areas are sintered by laser. The loose powder, which has not been fused serves as support material, which makes additional support of the parts unnecessary. This allows an efficient use of the build space, as the parts can be positioned three dimensionally. At the end of the build process, the sintered parts are encased in the build chamber with the surrounding powder as support material, which is often referred to as "part cake". Finally, after cooling, the parts are removed from the powder and cleaned. Unsintered powder can be sieved and reused for future print jobs [6].

Due to its many users and great potential, the SLS process is still a matter of interest in the research community [7, 8]. Polyamide 12 (PA12) is one of the materials commonly used in the SLS process [9]. Therefore, many scientific studies exist regarding the mechanical behavior of components made of PA12, which were manufactured by SLS [9–13]. However, in various investigations, it was found that some tensile specimens, which were tested according to DIN EN ISO 527-2, broke outside the parallel gage section [10, 14–17]. These samples differ in their mechanical behavior and are to be considered as invalid measurements considering the standard [17, 18]. It is not clear which mechanism triggers this behavior and how this effect can be avoided.

✉ J. Cronau
julius.cronau@unibw.de

1 Universität Der Bundeswehr (HAW), Werner-Heisenberg-Weg 39, 85577 Munich, Germany

2 Wehrwissenschaftliches Institut Für Werk- Und Betriebsstoffe (WIWeB), Institutsweg 1, 85435 Erding, Germany

The purpose of this study was to investigate the causes of this material behavior and which design factors and processing methods have an influence on this behavior. To investigate this, different tensile specimens were fabricated in build direction using SLS. In addition to the results from the quasi-static tensile tests, different surfaces of the specimens were analyzed before the tensile test using a 3D profilometer to determine a possible influence on the material behavior. In addition, the break surfaces were conducted for the same reason.

2 Materials and experimental procedure

2.1 Specimen fabrication

For the tests carried out, tensile specimens of type 1A were manufactured according to DIN EN ISO 527-2 using the SLS process, whereby the numbering of the specimens was introduced directly in form of an embossing on the clamping surface during the manufacturing process. The radius, which according to DIN EN ISO 527-2 must be 24 mm, has been varied between 14, 24, and 34 mm [17].

The specimens were manufactured on an EOS P396 SLS system (*EOS GmbH Electro Optical Systems, Krailing, Germany*) in different print jobs with different powder batches. All specimens were fabricated in a 90° orientation to the build platform, i.e., in build or Z direction, as shown in Fig. 1.

A parameter set from EOS was used for the manufacturing parameters of all specimens (PA2200 Balance 1.0—EOS). The build chamber temperature of the system was 172 °C and the temperature of the removal chamber was 130 °C. All samples were fabricated with a layer height of 120 μm from polyamide 12 (*PA12, PA2200 EOS GmbH*). To ensure process stability and repeatability, a blend of 50% used and 50% virgin semi-crystalline polyamide 12 powder was used as the sample material [19]. To ensure uniform crystallization and to avoid differences in the crystalline fraction between the sample batches, temperatures and cooling rates were kept the same for all build jobs [9]. The samples were de-powdered by glass bead blasting and compressed air. The total of 63 samples were then conditioned for at least a week in a standard climate (22 °C and 50% RH).
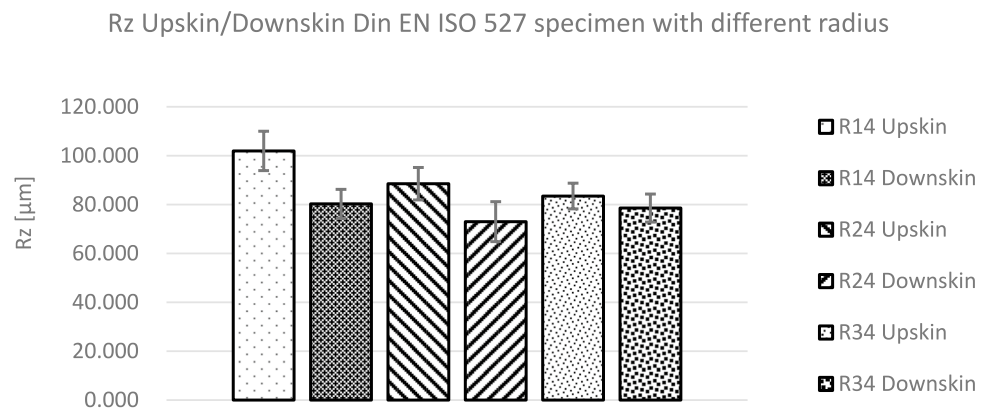
2.2 Testing methods

For the mechanical characterization of the specimens, a tensile test was carried out according to DIN EN ISO 527-1 and -2, whereby the cross-head speed was partially varied [17, 20]. Tests were performed at strain rates of 0.00022/s, 0.0022/s, 0.0044/s, 0.022/s, 0.044/s. The tests were carried out in a standard climate (23 °C, 50% RH). The tests were conducted on a universal testing machine Inspekt Table 50 (*Hegewald & Peschke Meß- und Prüftechnik GmbH, Nossen, Germany*), and the measurement of the change in length was performed by means of a video extensometer (*LIMESS Messtechnik u. Software GmbH, Krefeld, Germany*). The domain length of the video extensometer was 75 mm.

The surface was analyzed with an optical 3D profilometer VR-5000 (*Keyence Corporation, Osaka, Japan*). To ensure a comparable evaluation and the batch analysis of numerous samples, a jig was manufactured. This also ensured that the surface scans were always performed in the same position so that the measurement of the surface roughness and the profile measurements are performed at comparable positions. The evaluation of the surface roughness was done with the micro camera at 80-fold magnification. A stitching of 6 single images with a total size of 6 mm × 10 mm of each radius of 43 specimens was taken. In addition, measurements were made for comparative values at different magnifications as well as measuring some samples over the entire test area with radius.

For the measurement of surface roughness, according to DIN EN ISO 4288, the properties of the surface must first be known [20]. Because of the layer-by-layer buildup, a periodic surface profile can be assumed for an SLS specimen built in 90° direction, similar to that of turned parts.

Fig. 1 Results of the surface roughness measurements of the specimen with the different radii

Rz Upskin/Downskin Din EN ISO 527 specimen with different radius

- R14 Upskin
- R14 Downskin
- R24 Upskin
- R24 Downskin
- R34 Upskin
- R34 Downskin

Since the samples are manufactured at a layer thickness of 120 μm, it is reasonable to assume a periodic profile of 120 μm with deviations due to manufacturing tolerances. Using the VR-5000 optic 3D profilometer, an 80× magnification of the surface was scanned and the profile average of 30 profile lines spaced 5 μm apart was determined. This procedure ensures the measurement of the entire sample width except for the edges, where edge effects can occur. Individual defects only influence this method if they are present over a significant part of the sample width. In this case, the profile lines were at 90° to the layers. The profile average of one specimen is shown in Fig. 2.

It was found that periodic minima and maxima could be detected, but at about double the layer thickness of 240 μm. This value must be taken as a basis for the determination of the surface roughness in the next section.

Since the examination of the surface profiles did not reveal any apparent defects at the points where conspicuous fractures later occurred, the surface roughness was used as a comparative parameter. According to DIN EN ISO 4288, the relevant parameters are the center roughness R_a and the roughness depth R_z [20]. For the present case, R_z appears to be the suitable comparative parameter. Investigations have shown that a greater roughness depth correlates with the risk of stress peaks and thus with crack formation and failure of the component [23–25]. The surface roughness is measured according to DIN EN ISO 4288 [20]. A periodic roughness profile of RSm = 240 μm was used as a basis for determining the surface roughness. According to DIN EN ISO 4288, a single measuring section lr = 0.8 mm with a total measuring section of ln = 4 mm must be selected for the determination of the surface roughness for this RSm value [20]. The roughness measurement of the radii was performed with this setting.

The fracture surfaces were examined with a scanning electron microscope (SEM) ZEISS EVO LS25 (*Carl Zeiss AG, Oberkochen, Germany*) where conspicuous features were first detected by visual inspection, which were then examined in the SEM. The images were taken with a voltage of 20 kV at a chamber pressure of 30 pa by the WIWeB GF310 department.

3 Results and discussion

3.1 Surface profiling

Before performing the tensile tests, the surface of the specimens was scanned at the radii. This data was examined for imperfections that could indicate a later stress concentration. No such flaws were found in the areas where the fractures occurred. However, the measurements were complicated by the high number of fused powder grains on the surface. These ranged in diameter from 16 to 100 μm, with the majority of particles between 37.5 and 63 μm which are similar results to than in other research [21, 22].

3.2 Surface roughness

For the specimen with the radius of 14 mm, R_z is about 20% higher in the upskin radii than in the downskin radii over all measured samples (Fig. 1). The differences between the R_z in the upskin radii and the downskin radii are getting less with higher radii (Fig. 1). This effect can be explained by the shrinkage of the individual layers after exposure. Figure 3 shows a surface measurement (B) from an edge lying at the bottom in the build direction in the component, and (A) from an edge lying at the top in the build direction. While the latter is slightly warped upward due to shrinkage and therefore has a sharp edge, the former is more rounded because the bottom edge is rounded by warping. In combination with the staircase effect typical for additive manufacturing, this results in a sequence of sharp edges in the upskin surface and subsequently a sequence of round edges in the downskin surface, which leads to different R_z values. As expected, the difference in R_z between upskin and downskin surfaces decreases with increasing radius (Fig. 4).

The larger the angle of the upskin surface relative to the build platform, the smaller the stair step effect and consequently also the difference in roughness.
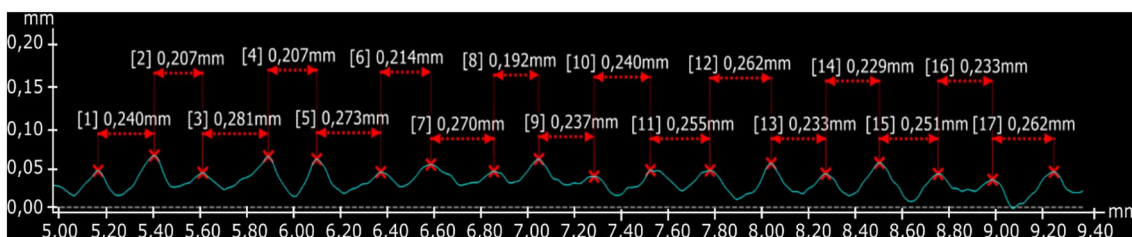

Fig. 2 Surface profile measured in build direction on the surface of the specimen. The profile represents the average of 30 individual profile lines spaced 5 μm apart
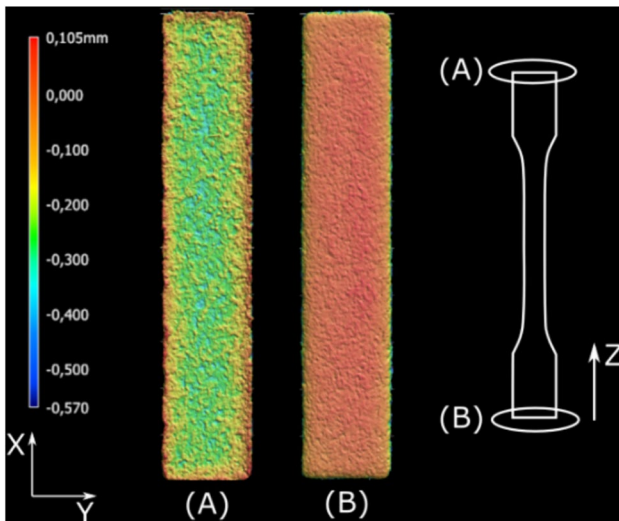
Fig. 3 Sharp edge on the upskin surface of the specimen (**A**), round edge on the downskin surface (**B**)

3.3 Tensile test

The tensile tests were performed in three batches, named 0, 1, 2. Batch 0 consisted of 20 specimens with the same radius $R = 24$ mm but varying strain rates. Batch 1 consisted of 13 specimens, with radius and post-processing varied. The strain rate was kept constant at 0.024/s. Batch 2 consisted of 30 specimens where the radii were also varied. The strain rate for batch 2 was 0.024/s, the same as for batch 1. Large variations were observed across all batches, particularly in the strain at break of the individual specimens. The number of out-of-break specimens differed greatly from batch to batch. Both Young's modulus and tensile strength varied little across batches. It can be concluded that the SLS components exhibit relatively consistent properties in the build direction. The only exception is the elongation at break, which varies greatly both within and between batches. In batch 2, for example, the lowest elongation at break was ~5% and the highest was ~21% (Fig. 5). Figure 5 shows the stress–strain curves of the tensile tests for batch 2 radius 24 mm.

3.4 Fractography

After the tensile test, some fracture surfaces were examined where either a fracture outside the test range or a particularly low elongation at break occurred. Here, additional findings could be collected. All fracture surfaces showed different areas in the SEM image (Fig. 6). The fracture surfaces of the specimen R24-5 with particularly low fracture elongation (Fig. 6B, E) show a porous, poorly sintered edge in which the individual powder particles are not completely molten. This can be seen in Fig. 6B1. A closer look at this area in
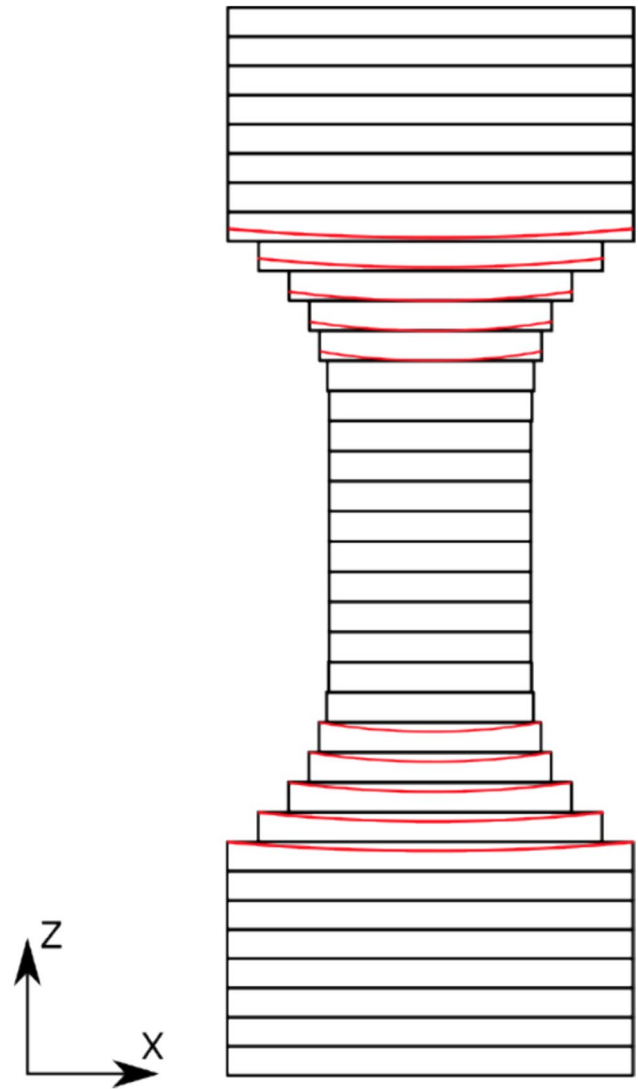

Fig. 4 Schematic representation of the layers in up and downskin surfaces

Fig. 6E shows two different types of defects. Figure 6E1 shows large pores under the surface and a comparably wide area from unsintered surface particles to the solid part. Figure 6E2 shows a large amount of unmolten powder particles in the specimen. Figure 6E3 shows filamentary structures indicating ductile deformation of the polymer chains in these areas. In can be concluded that the crack initiation of the specimen seen in Fig. 6B and E was on the surface. After the crack initiated, a small area of ductile failure can be seen (Fig. 6E3) before a brittle failure can be seen in Fig. 6B3. In comparison, Fig. 6C and F shows the break surface of specimen R24-4 with high elongation at break. No areas with unsintered powder particles were found here. The surface in Fig. 6C1 do not show large pores in this specimen. The area of ductile failure Fig. 6C2 begins right next to the surface area. Here also an area of brittle fracture can be seen
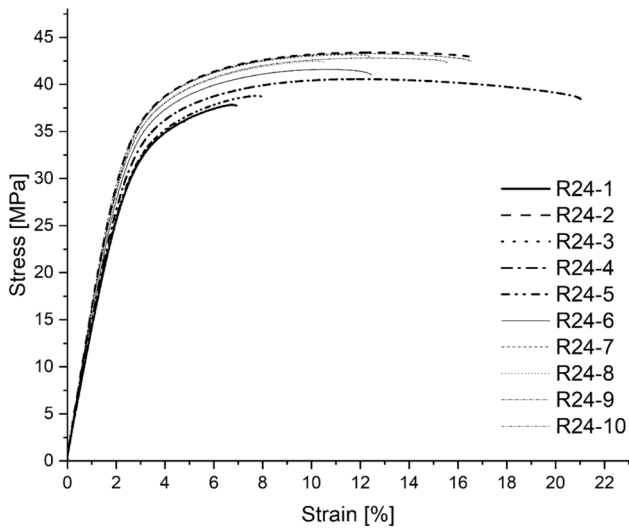
Fig. 5 Stress–strain diagram of batch 2 R24. Especially the elongation at break and the tensile strength show large derivations

(Fig. 6C3). The specimen which broke outside the test area R24-7 (Fig. 6A, D) does not show a significant difference to the specimen with high elongation at break (Fig. 6C, E). No areas with unmolten powder particles were found within the fracture surface. The three distinct areas are also present here. In Fig. 6D1, the surface area with unsintered powder particles can be seen. One area of the fracture surface also shows filamentary structures which indicate ductile fracture (Fig. 6D2). Figure 6D3 shows an area of brittle fracture, which can also be seen in Fig. 6A.

Table 1 shows the fracture strains and roughness values in the upskin radii associated with the samples examined in the SEM. The specimen which is broken outside the test area has a significantly higher surface roughness than the other specimens. It should be noted that the elongation at break of this sample R24-7 cannot be determined accurately due to the fracture outside the test area. Based on the images, it can be concluded that none of the specimen showed a pure brittle fracture. The defects in the marginal areas of the pores lead to a stress peak and a crack develops here, which is soon followed by ductile material behavior. If the stress increases further, a fracture of the specimens occurs. The specimens show uniformly distributed pores in the fracture surfaces, similar to previous investigations. [13, 26].

Table 1 Measured fracture strain and roughness values of the samples examined in SEM

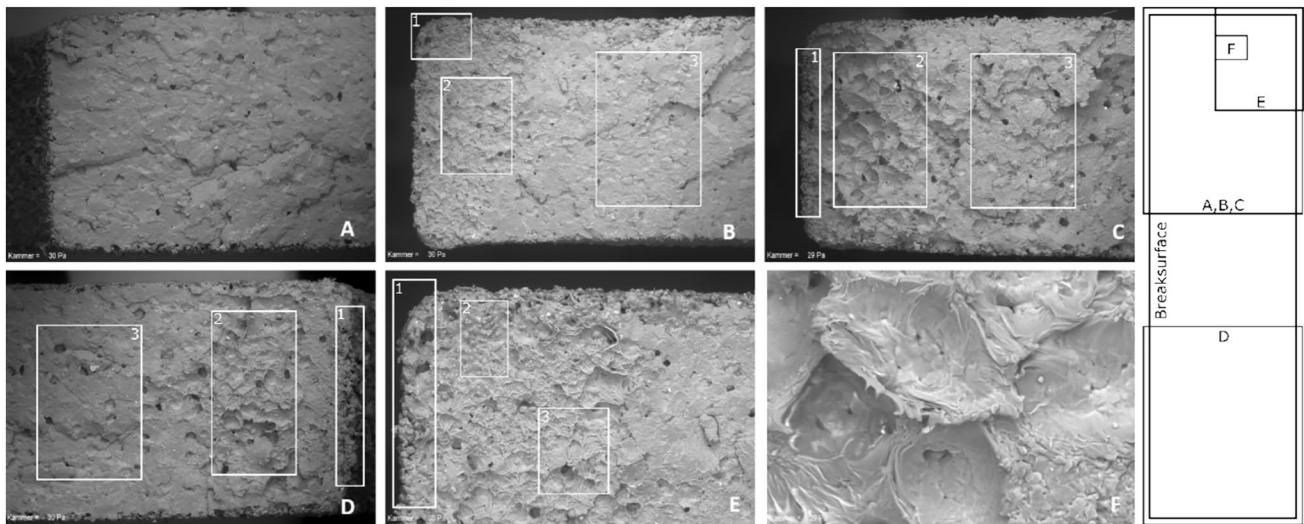| Specimen	R_z upskin (μm)	ε_b (%)	Characteristic at break
R24-4	91,144	21.2	Mixed
R24-5	80,263	8.04	Mixed—defects in break surface visible in SEM
R24-7	104,911	–	Mixed—break outside test area

Fig. 6 SEM of the break surface of three different specimen: **A**, **D** break outside the test area, edge area D, filamentary structures D2, brittle fracture surface D3; **B**, **E** low elongation at break, large surface pores E1, unsintered particles in the surface in E2, filamentary structures B2, E3; **C**, **F** high elongation at break, small edge area C1, no unmolten particles, large ductile area C2, Area of brittle Fracture C3; F shows ductile area in detail

4 Conclusion

Tensile tests were performed to investigate the effect of tensile specimens built in Z direction breaking outside the test area as well as the high differences in the elongation at break. For this purpose, the radii of the tensile specimens were determined before the tensile test and the surface profile as well as the roughness R_z was evaluated. In addition, the fracture surfaces of the specimens that either broke outside the test area or exhibited a particularly low or high elongation at break were examined with a SEM.

It was not possible to predict from the surface profile at which point the specimens would fracture or whether there would be a defect on the surface. This was because of the large amount of powder particles fused onto the surface of the specimen. It was found that the upskin surfaces had a greater roughness depth R_z than the downskin surfaces. This is a consequence of the process-related shrinkage during solidification of the melt. This effect increases with smaller angles relative to the build platform. SEM images were taken of the fracture surfaces of the specimens with particularly low or high elongation and of specimens which fractured outside the test area. The specimens with particularly low elongation showed a comparatively large area of poorly sintered powder particles and a large transition area between the completely fused area and fused edge particles. In these areas, large notches and irregularities in the edge surface as well as the aforementioned poorly sintered areas were found to be the starting point for cracks and, thus, the low fracture elongation. The porches with high fracture elongation showed fewer defects of this type. Specimen that broke outside the test area did not show these defects. The differences in surface roughness between the upskin and downskin radii could be an explanation why the breaks outside the test area only occur in the upskin area. However, further tests are necessary to quantify this effect. The shrinkage which leads to the different roughness values could also lead to residual stresses which could also be an explanation for the break outside the test area in the upskin radii. Further investigations, such as residual stress measurements, digital image correlation (DIC) or process monitoring with a thermal imaging camera, are necessary to determine the final cause of the problem.

References

1. Dizon JRC, Espera AH, Chen Q, Advincula RC (2018) Mechanical characterization of 3D-printed polymers. Addit Manuf 20:44–67. https://doi.org/10.1016/j.addma.2017.12.002

2. Javaid M, Haleem A, Singh RP, Suman R, Rab S (2021) Role of additive manufacturing applications towards environmental sustainability. Adv Ind Eng Polym Res 4(4):312–322. https://doi.org/10.1016/j.aiepr.2021.07.005

3. Praveena BA, Lokesh N, Buradi A, Santhosh N, Praveena BL, Vignesh R (2022) A comprehensive review of emerging additive manufacturing (3D printing technology): methods, materials, applications, challenges, trends and future potential. Mater Today Proc 52:1309–1313. https://doi.org/10.1016/j.matpr.2021.11.059

4. Calignano F, Giuffrida F, Galati M (2021) Effect of the build orientation on the mechanical performance of polymeric parts produced by multi jet fusion and selective laser sintering. J Manuf Process 65:271–282. https://doi.org/10.1016/j.jmapro.2021.03.018

5. Tan LJ, Zhu W, Zhou K (2020) Recent progress on polymer materials for additive manufacturing. Adv Funct Mater 30(43):2003062. https://doi.org/10.1002/adfm.202003062

6. Goodridge RD, Tuck CJ, Hague R (2012) Laser sintering of polyamides and other polymers. Prog Mater Sci 57(2):229–267. https://doi.org/10.1016/j.pmatsci.2011.04.001

7. Wang R-J, Wang L, Zhao L, Liu Z (2007) Influence of process parameters on part shrinkage in SLS. Int J Adv Manuf Technol 33(5–6):498–504. https://doi.org/10.1007/s00170-006-0490-x

8. Xu Z, Wang Y, Wu D, Ananth KP, Bai J (2019) The process and performance comparison of polyamide 12 manufactured by multi jet fusion and selective laser sintering. J Manuf Process 47:419–426. https://doi.org/10.1016/j.jmapro.2019.07.014

9. Kiani A, Khazaee S, Badrossamay M, Foroozmehr E, Karevan M (2020) An investigation into thermal history and its correlation with mechanical properties of PA12 parts produced by selective laser sintering process. J Mater Eng Perform 29(2):832–840. https://doi.org/10.1007/s11665-020-04640-0

10. Caulfield B, McHugh PE, Lohfeld S (2007) Dependence of mechanical properties of polyamide components on build parameters in the SLS process. J Mater Process Technol 182(1–3):477–488. https://doi.org/10.1016/j.jmatprotec.2006.09.007

11. Hofland EC, Baran I, Wismeijer DA (2017) Correlation of process parameters with mechanical properties of laser sintered PA12 parts. Adv Mater Sci Eng 2017(5):1–11

12. Puttonen T, Salmi M, Partanen J (2021) Mechanical properties and fracture characterization of additive manufacturing polyamide 12 after accelerated weathering. Polym Testing 104:107376. https://doi.org/10.1016/j.polymertesting.2021.107376

13. Tomanik M, Żmudzińska M, Wojtków M (2021) Mechanical and structural evaluation of the PA12 desktop selective laser sintering

printed parts regarding printing strategy. 3D Print Addit Manuf 8(4):271–279. https://doi.org/10.1089/3dp.2020.0111

14. Krönert M, Schuster TJ, Zimmer F, Holtmannspötter J (2022) Creep behavior of polyamide 12, produced by selective laser sintering with different build orientations. Int J Adv Manuf Technol 121:3285–3294

15. Wroe WW (2015) Improvements and effects of thermal history on mechanical properties for polymer selective laser sintering (SLS): MA Texas. Master thesis, The University of Texas at Austin

16. Ahn S-H, Montero M, Odell D, Roundy S, Wright PK (2002) Anisotropic material properties of fused deposition modeling ABS. Rapid Prototyp J 8(4):248–257. https://doi.org/10.1108/13552 540210441166

17. DIN EN ISO 527–2:2012–06, Plastics—determination of tensile properties—part 2: test conditions for moulding and extrusion plastics (ISO_527–2:2012), Deutsches Institut für Normung, Berlin

18. DIN EN ISO 527–1, Plastics—determination of tensile properties. Part 1, General principles (ISO 527–1:2019): plastics—determination of tensile properties. Part 1, General principles (ISO 527–1:2019), Deutsches Institut für Normung, Berlin

19. Dadbakhsh S, Verbelen L, Verkinderen O, Strobbe D, van Puyvelde P, Kruth J-P (2017) Effect of PA12 powder reuse on coalescence behaviour and microstructure of SLS parts. Eur Polymer J 92:250–262. https://doi.org/10.1016/j.eurpolymj.2017.05.014

20. DIN EN ISO 4288:1998–04, Geometrical product specifications (GPS)—surface texture: profile method—terms, definitions and surface texture parameters (ISO_4288:1996); German version EN_ISO_4288:1997, Deutsches Institut für Normung, Berlin

21. Berretta S, Ghita O, Evans K, Anderson A, Newman C (2013) Size, shape and flow of powders for use in selective laser sintering (SLS). In: Da Bartolo PJS et al (eds) High value manufacturing: proceedings of the 6th international conference on advanced research in virtual and rapid prototyping, Leiria, Portugal, 1–5 Oct 2013. Taylor and Francis, Hoboken, pp 49–54

22. Schneider J, Kumar S (2020) Multiscale characterization and constitutive parameters identification of polyamide (PA12) processed via selective laser sintering. Polym Testing 86:106357. https://doi.org/10.1016/j.polymertesting.2020.106357

23. de Oliveira SG, de Oliveira MF, Maia IA, Da Silva JVL, Savu R, Joanni E (2014) Correlation between mechanical and surface properties of SLS parts. Rapid Prototyp J 20(4):285–290. https://doi.org/10.1108/RPJ-08-2012-0070

24. Evans NT, Irvin CW, Safranski DL, Gall K (2016) Impact of surface porosity and topography on the mechanical behavior of high strength biomedical polymers. J Mech Behav Biomed Mater 59:459–473. https://doi.org/10.1016/j.jmbbm.2016.02.033

25. Zhang J, Fatemi A (2019) Surface roughness effect on multiaxial fatigue behavior of additive manufactured metals and its modeling. Theoret Appl Fract Mech 103:102260. https://doi.org/10.1016/j.tafmec.2019.102260

26. Stichel T et al (2017) A Round Robin study for selective laser sintering of polyamide 12: microstructural origin of the mechanical properties. Opt Laser Technol 89:31–40. https://doi.org/10.1016/j.optlastec.2016.09.042